ACS APPLIED MATERIALS & INTERFACES

Research Article

www.acsami.org

Electron Collection in Host–Guest Nanostructured Hematite Photoanodes for Water Splitting: The Influence of Scaffold Doping Density

Ilina Kondofersky,[⊥,†] Halina K. Dunn,[⊥,†] Alexander Müller,[‡] Benjamin Mandlmeier,[†] Johann M. Feckl,[†] Dina Fattakhova-Rohlfing,[†] Christina Scheu,[‡] Laurence M. Peter,[§] and Thomas Bein*[,†]

[†]Department of Chemistry and Center for NanoScience (CeNS), Ludwig-Maximilians-Universität München, Butenandtstr. 5-11, D-81377 Munich, Germany

[‡]Max-Planck-Institut für Eisenforschung GmbH, Max-Planck-Straße 1, 40237 Düsseldorf, Germany

[§]Department of Chemistry, University of Bath, BA2 7AY, Bath, United Kingdom

Supporting Information

ABSTRACT: Nanostructuring has proven to be a successful strategy in overcoming the trade-off between light absorption and hole transport to the solid/electrolyte interface in hematite photoanodes for water splitting. The suggestion that poor electron (majority carrier) collection hinders the performance of nanostructured hematite electrodes has led to the emergence of host–guest architectures in which the absorber layer is deposited onto a transparent high-surface-area electron collector. To date, however, state of the art nanostructured hematite electrodes still outperform their host–guest counterparts, and a quantitative evaluation of the benefits of the host–guest architecture is still lacking. In this paper, we examine the impact of host–guest architectures by comparing nanostructured tin-doped hematite electrodes with hematite nanoparticle layers coated onto two types of conducting macroporous SnO_2 scaffolds. Analysis of the external quantum efficiency spectra for substrate (SI) and electrolyte side (EI) illumination reveals that the electron diffusion length in the host–guest electrodes based on an undoped SnO_2 scaffold is increased substantially relative to the nanostructured hematite electrode without a supporting scaffold. Nevertheless, electron collection is still incomplete for EI illumination. By contrast, an electron collection efficiency of 100% is achieved by fabricating the scaffold using antimony-doped SnO_2, showing that the scaffold conductivity is crucial for the device performance.

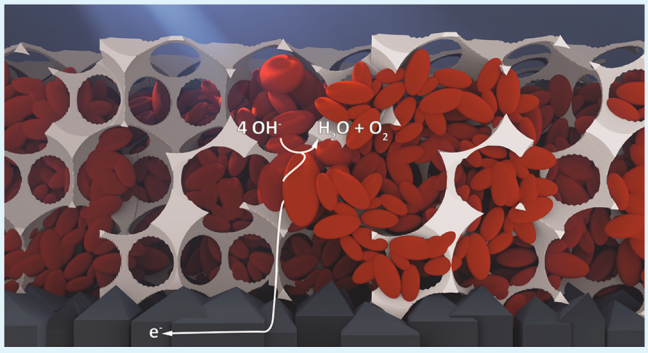

KEYWORDS: *photoelectrochemical water splitting, host–guest, effective electron diffusion length, iron oxide, antimony-doped SnO_2*

INTRODUCTION

The demand for alternative energy resources has intensified research on photoelectrochemical systems for water splitting as a sustainable hydrogen source. Among the many semiconductors studied as possible candidates,[1−3] α-Fe_2O_3 hematite has received particular attention due to its chemical stability in basic solutions, its abundance and low production costs, in addition to a theoretical maximum solar-to-hydrogen efficiency of around 16% in a tandem configuration in combination with a low band gap solar cell.[1,4,5]

One of the attractive features of hematite is that it absorbs light in the visible range up to a wavelength of around 600 nm. However, considering the small hole diffusion length in hematite of only 2–4 nm,[6] only holes photogenerated in the space charge region are likely to take part in the oxygen evolution reaction at the surface, while those generated in the bulk are mostly lost to recombination.[7] These wasteful effects become increasingly significant for longer wavelengths, where most electron hole pairs are generated outside of the space charge region. One of the ways to improve the total charge collection efficiency of hematite photoanodes is nanostructuring, which addresses the trade-off between sufficient light harvesting and efficient hole collection by decoupling the hole collection depth from the light absorption depth. However, besides the increased photocurrents observed for different hematite nanomorphologies,[8−14] nanostructuring also brings drawbacks such as longer and more tortuous paths for the transport of majority charge carriers (electrons) to the current collector, increasing the probability of their recombination with holes. Furthermore, the higher surface area can lead to additional electron recombination losses with species such as surface trapped holes and intermediates formed during the

Received: November 12, 2014
Accepted: January 6, 2015
Published: January 6, 2015

DOI: 10.1021/am5078667
ACS Appl. Mater. Interfaces 2015, 7, 4623−4630

oxygen evolution reaction (OER). An alternative approach aiming to combine the advantages of both thin layer and nanostructured morphologies without the above-mentioned limitations is the fabrication of hierarchical electrodes, in which the hole transport and the electron collection pathways are effectively decoupled from each other. In such electrodes (also called host−guest architectures (HGA)), thin hematite layers are deposited on current collecting scaffolds with a high surface area.[14−18] The current collector should be a wide band gap material with good electron transport properties and a suitable conduction band alignment to the hematite absorber so as to allow rapid electron extraction at the contact. Suitable scaffold materials include transparent conducting oxides (TCO) and semiconducting metal oxides.

Several studies have demonstrated the feasibility of the HGA concept for water splitting.[16−25] Sivula et al. were the first to demonstrate the suitability of WO_3 as an electron-extraction scaffold for hematite, although the enhancement in photocurrent was modest due to the low surface area of the WO_3 layers.[16] Several authors have convincingly demonstrated that thin absorber layers deposited on high surface area current collectors generate photocurrents that are substantially higher than those measured for the same layers on a flat substrate.[20,21] However, the host−guest concept has not yet delivered the promise of improved water splitting performance. Despite intensive research activity in this area, state of the art host−guest hematite-based photoanodes have, surprisingly, not yet outperformed their nanostructured hematite counterparts. Although significant currents have been reported for different host−guest systems, such as 0.25 $mAcm^{-2}$ or 1 $mAcm^{-2}$ at 1.23 V versus RHE for thin layer hematite deposited on inverse opal indium tin oxide electrodes[20] or porous niobium doped tin oxide,[21] respectively, these HGA electrodes did not reach the efficiency of the best nanostructured electrodes (such as uncatalyzed Si-doped hematite prepared by APCVD, which has reached 1.8 $mAcm^{-2}$ under standard conditions at 1.23 V vs RHE under AM 1.5 illumination).[14]

A central objective of this work was the investigation of host−guest hematite architectures in water oxidation reactions aimed at understanding the factors that determine their efficiency. For this purpose, we have studied the photoelectrochemical activity of nanostructured tin-doped hematite absorber layers deposited from precursor solutions. These films were fabricated on flat FTO substrates as well as on two types of macroporous SnO_2 scaffolds with similar morphology but different electrical conductivity. Because improved electron collection is usually considered the main factor governing the performance of host−guest electrodes, we have compared the electron diffusion length for nanostructured tin-doped hematite layers and the same layers coated on macroporous SnO_2 and Sb-doped SnO_2 host scaffolds with different conductivity. The electron diffusion length was determined from the spectral dependence of the ratio of the external quantum efficiency (EQE) for illumination through the electrolyte (EI) and through the substrate (SI). On the basis of the analysis of the EQE spectra for EI and SI illumination, we demonstrate that the deposition of the hematite layer on an undoped SnO_2 scaffold increases the electron collection efficiency significantly, although electron collection is still incomplete for EI illumination. However, when Sb-doped SnO_2 is used, complete collection of electrons occurs, and EI and SI EQE spectra are identical.

EXPERIMENTAL SECTION

Synthesis and Deposition of Poly(methyl methacrylate) (PMMA) Spheres. Poly(methyl methacrylate) (PMMA) spheres with a diameter of 300 nm were prepared according to a procedure described by Mandlmeier et al.[26] The particles were synthesized by adding methyl methacrylate (MMA) (35.6 g, 0.35 mol) and sodium dodecyl sulfate (SDS) (5 mg, 0.02 mmol) to deoxygenated water (98 mL) under nitrogen purging at 40 °C, heating the resulting emulsion to 70 °C for 1 h under reflux, and vigorous stirring. The polymerization was then initiated by adding potassium peroxydisulfate (56 mg, 0.2 mmol) in water (2 mL) and carried out for 2.5 h. The reaction was stopped by cooling the suspension to room temperature and stirring for another 30 min under atmospheric conditions. The resulting PMMA spheres were washed twice with water by centrifugation (19 000 rpm, 20 min) and redispersed in water.

Deposition of PMMA spheres on FTO substrates (TEC 15 Glass, Dyesol) was carried out by ultraslow dip coating (0.45 mm/min) of a 5 wt % PMMA suspension at 19% relative humidity, using a custom-made coater connected to a humidity control box. The resulting films were dried in a nitrogen stream and heated to 80 °C for 2 h to increase adherence between the PMMA spheres (Figure S 1).

Preparation of Macroporous SnO_2 Films. The precursor solution for macroporous SnO_2 was prepared according to Fried et al.[27] by adding 4 mL dry ethanol dropwise to $SnCl_4$ (1.2 g, 4.6 mmol, in air). Deionized water (0.5 mL, Millipore Q) was then added resulting in a 0.15 M $SnCl_4$ solution. This solution was dip-coated on previously prepared PMMA films under ambient conditions at a rate of 38 mm/min. The samples were subsequently calcined at 600 °C with a ramp of 3 °C/min and a dwell time of 30 min. Figure S 2 shows SEM images of such macroporous films.

Preparation of Antimony-Doped Macroporous SnO_2 Films. For the preparation of the Sb-doped SnO_2 samples, $Sb(AcO)_3$ (0.0672 g, 0.2 mmol) was added to 4 mL of ethanol prior to adding $SnCl_4$ (1.14 g, 4.4 mmol). The subsequent steps were followed as described above for SnO_2. The Sb/Sn ratio refers to the atomic ratio of these elements in the precursor solution. For further film synthesis, an identical procedure was used as already described for the undoped films. Figure S 3 shows the XRD analysis of macroporous SnO_2 and SnO_2:Sb films.

Synthesis and Deposition of Tin-Doped Hematite on FTO and Macroporous SnO_2. A suspension of tin-doped hematite nanoparticles was synthesized as described by Dunn et al.[28] Briefly, 0.1106 g (0.3 mmol) of $Sn(CH_3COO)_4$ was added to a solution of 0.25 g of Pluronic P123 and 10 mL of *tert*-butanol. After vigorous stirring for 5 h, 0.505 g (1.25 mmol) of $Fe(NO_3)_3{\cdot}9\,H_2O$ was added and stirred at room temperature for another 15 min. After sonication for 15 min, 2.5 mL of water was added, and the solution was stirred for 17 h at room temperature. After filtration through a filter (pore diameter of 200 nm), the solution was ready for coating experiments. For preparation of flat Sn-containing hematite films, the solution (100 μL) was spun on FTO at 1000 rpm for 30 s. The resulting films were dried at 60 °C for 10 min and calcined at 600 °C with a ramp of 3 °C/min and a dwell time of 30 min. Typically, the filtered solution (100 μL) was cast on the macroporous scaffold (1 × 1 cm^2), spun at 1000 rpm for 30 s, and finally dried at 60 °C for 10 min. To achieve an increased precursor loading, the previous step was repeated twice. After spin coating, the samples were calcined at 600 °C with a ramp of 3 °C/min and a dwell time of 30 min. Figure S 4 shows an SEM image of a tin-doped hematite film deposited on FTO with the corresponding XRD pattern after calcination. The feature size of the tin-doped hematite absorber material was determined to be around 50 nm from TEM particle size analysis (Figure S 5).

Synthesis and Deposition of Tin-Doped Hematite on Macroporous Silica (SiO_2) Films. Macroporous silica (SiO_2) films were prepared according to the sol−gel route reported by Schuster et al.[29] Briefly, 6 mL of tetraethyl orthosilicate (TEOS) was dissolved in ethanol and stirred for 5 min; upon adding 3 mL of water to the solution, a phase separation was observed. One milliliter of 37% HCl was added and the solution became clear. The resulting solution was used as a precursor for dip coating PMMA films at 34 mm/min.

DOI: 10.1021/am5078667
ACS Appl. Mater. Interfaces 2015, 7, 4623−4630

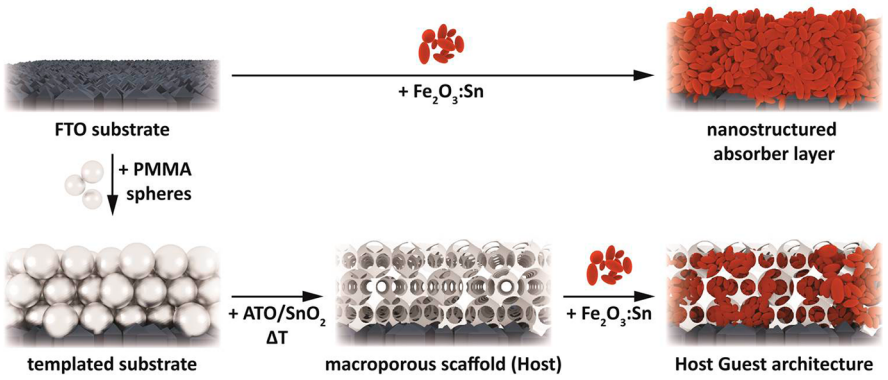

Figure 1. Synthesis scheme of macroporous host–guest samples and nanostructured flat absorber films on FTO.

Subsequently the samples were calcined at 500 °C (1 °C/min) for 5 h. These samples were then infiltrated with tin-doped hematite as already described for macroporous SnO_2:Sb. Figure S 6a shows an SEM image of the macroporous silica scaffold. Image SI 6b shows the photocurrent collected from the tin-doped hematite nanoparticles on the silica scaffold.

Preparation of Flat SnO_2 and SnO_2:Sb Films for Electrochemical Impedance Spectroscopy Measurements. Flat and compact SnO_2 and SnO_2:Sb films, as shown in Figure S 7, were prepared using the corresponding precursor solution described for the synthesis of macroporous scaffolds. The solution was deposited on FTO by spin coating at 1000 rpm for 30 s. The samples were calcined at 600 °C with a ramp of 3 °C/min and a dwell time of 30 min.

Characterization. X-ray diffraction analysis was carried out in reflection mode using a Bruker D8 diffractometer operating at 40 kV and 40 mA with Ni-filtered Cu Kα radiation (wavelength: 1.5406 Å) with theta/theta geometry. Scanning electron microscopy (SEM) measurements were performed on a JEOL JSM-6500F scanning electron microscope using a 5 kV field emission gun and an Oxford energy dispersive X-ray (EDX) spectroscopy detector. Transmission electron microscopy (TEM) was performed on an FEI Titan TEM/STEM 80–300 equipped with a field-emission gun operated at 300 kV. Bright field (BF) and high-resolution (HR) TEM images as well as electron diffraction patterns were recorded with a Gatan UltraScan CCD camera with 2000 × 2000 pixels, and high angle annular dark field scanning TEM (HAADF-STEM) images were taken with a Fischione Instruments (Model 3000) detector. For EDX measurements, an EDAX detector was used.

The TEM samples were prepared in two ways. For an initial analysis of the structures, material was scraped off the FTO substrate using a razor blade and deposited on a copper grid with a holey carbon film. In addition, a cross-section was prepared according to a procedure established by Strecker et al.[30] EDX maps were plotted using the Fe–K and the Sn–L signals.

Sample thickness and homogeneity of films was measured with a profilometer using a Vecco (Dektak 156) with a 640 × 489-pixel camera and a diamond tip (radius 12.5 μm).

UV–vis measurements were performed on a PerkinElmer Lambda 1050 UV/Visible/NIR spectrophotometer with an integrating sphere. The absorbance of each sample was calculated from experimental reflectance and transmittance data,[31] using the expression

$$\mathrm{Abs_F} = \ln\left(\frac{T_{S+F}/T_S}{1 - \frac{R_{S+F} - R_S}{T_S^2}}\right) \quad (1)$$

Here T_S/T_{S+F} and R_S/R_{S+F} correspond to the wavelength dependent transmissions and the reflections of the FTO substrate and the film-coated substrate, respectively.

Photoelectrochemical Characterization. Photoelectrochemical characterization was carried out using a μ-Autolab III potentiostat equipped with a FRA2 impedance analyzer. The samples were masked with a Teflon-coated glass fiber adhesive tape, leaving an area of 0.2 cm^2 free for illumination. Samples were placed in a quartz cell filled with electrolyte (aqueous 0.1 M NaOH solution) and connected in three-electrode mode, together with the Ag/AgCl reference electrode and the Pt mesh counter electrode, to the potentiostat. The films were then illuminated either through the substrate (SI) or the electrolyte (EI) side using an AM 1.5 solar simulator (Solar Light Model 16S) at 100 mW cm^{-2}.

Current–voltage (I–V) curves were obtained by scanning from negative to positive potentials in the dark or under illumination at a 20 mV/s sweep rate. The photocurrent is defined as the difference between the light and dark current.

External quantum efficiency (EQE) measurements shown in Figure S 9 were performed under low-frequency chopped monochromatic light (1 Hz). A 150 W xenon lamp equipped with a monochromator and order-sorting filters was used as a light source. The sample bias was set to 1.23 V vs RHE under simulated solar irradiation to ensure realistic operating conditions. The light intensity was measured at the position of the electrode inside the cells using a 4 mm^2 photodiode, which had been calibrated against a certified Fraunhofer ISE silicon reference cell equipped with a KG5 filter.

RESULTS AND DISCUSSION

The inverse opal host–guest electrodes used in this work were fabricated via colloidal crystal templating (Figure 1).[32] The inverse opal morphology features uniform open pores that can be coated internally with the absorber material. The periodic network of interconnected walls is intended to act as a continuous pathway for electron transport to the anode contact. In a typical procedure, a template opal film was prepared by deposition of 300 nm poly(methyl methacrylate) (PMMA) spheres on an FTO substrate via ultraslow dip coating resulting in an ordered close packing of spheres. Afterwards, the opal films were impregnated with a sol–gel oxide precursor via dip coating and calcined in air to remove the PMMA template. Two types of scaffolds with identical morphology but different electrical conductivity of the walls were prepared, namely, tin oxide (SnO_2) and antimony-doped tin oxide (SnO_2:Sb). Additionally, insulating silica inverse opal layers were used to investigate the role of the scaffold conductivity on the performance of host–guest electrodes.

The macroporous SnO_2 and SnO_2:Sb scaffolds obtained after calcination are composed of interconnected periodically ordered spherical pores with a diameter of 250 nm separated by ca. 30–40 nm thick crystalline pore walls and interconnected by openings around 80 nm in diameter. The size of the pores after calcination is about 17% smaller than the diameter of the parent PMMA beads due to the crystallization-induced shrinkage of the inorganic scaffold. The average thickness of the calcined films is about 2 μm. The donor doping

DOI: 10.1021/am5078667
ACS Appl. Mater. Interfaces 2015, 7, 4623–4630

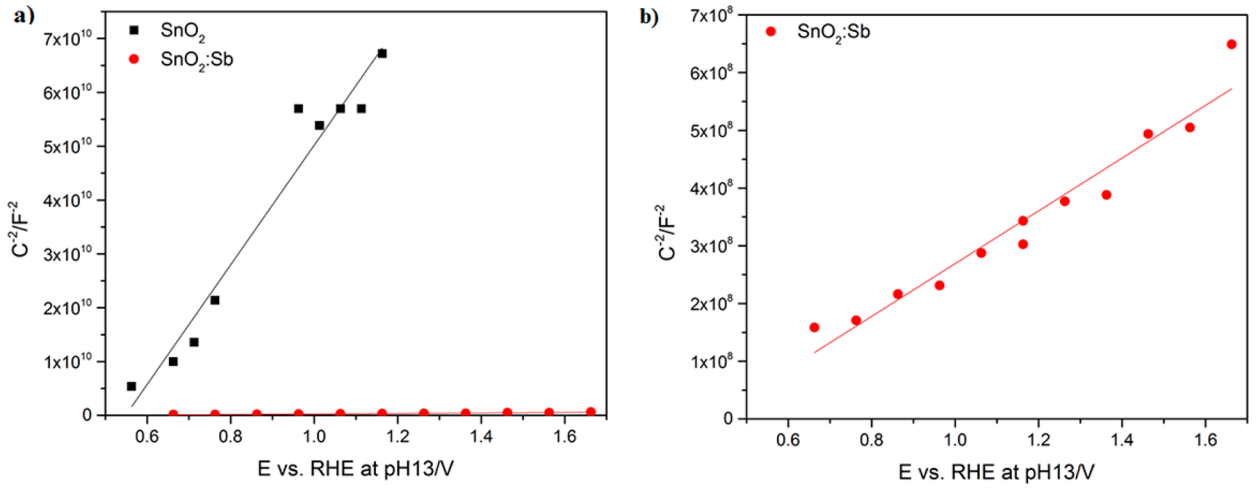

Figure 2. Capacitance data plotted in Mott–Schottky representation for SnO_2:Sb and SnO_2 flat layers coated on FTO (a); (b) shows the plot for ATO at a different scale. Electrolyte 0.1 M NaOH, electrode area 0.2 cm^2.

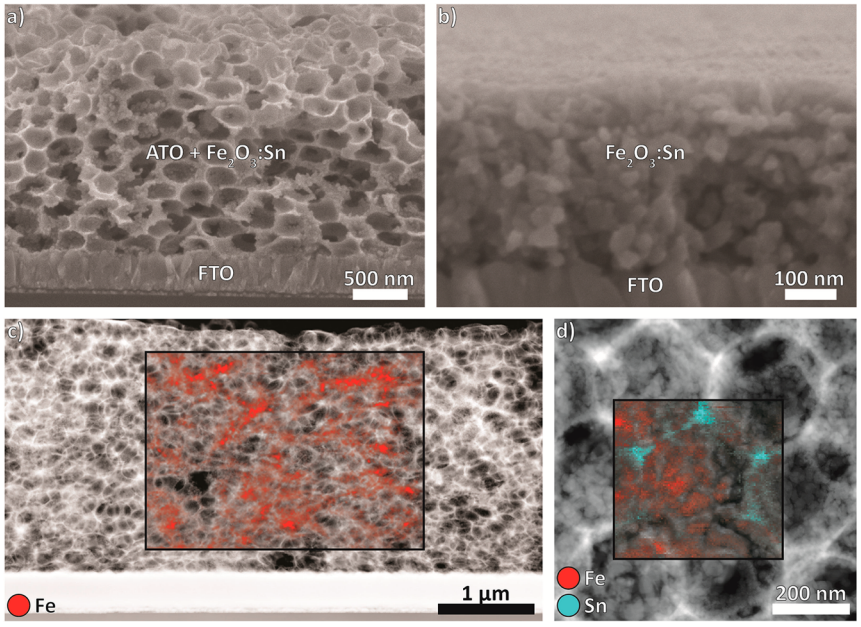

Figure 3. SEM cross section images of (a) the SnO_2:Sb (ATO) + Sn:Fe_2O_3 host–guest morphology and (b) the mesoporous Sn:Fe_2O_3 absorber layer. In (c) and (d), EDX maps obtained in STEM mode on a cross section of the host–guest morphology are shown with red signifying tin-doped hematite and turquoise signifying SnO_2:Sb. (c) shows good infiltration of the absorber in the scaffold down to the bottom, although some pores remain unfilled, and (d) shows one pore in which several hematite nanoparticles can be seen. Both the TEM and SEM image show a three layer Sn:Fe_2O_3 film.

density, estimated from the Mott–Schottky analysis of compact layers of SnO_2 and SnO_2:Sb (Figure 2), increases by around 3 orders of magnitude upon Sb doping, confirming that the latter acts as an electrical dopant (see Figure S 10 for further details).[17]

To fabricate working photoanodes, the macroporous structures were infiltrated with tin-doped hematite by spin coating the precursor solution, as summarized in Figure 1. The procedure for fabrication of nanostructured tin-doped hematite coatings on fluorine-doped tin oxide coated glass substrates via a solution-based method has been described by us elsewhere.[28] In a typical procedure, a precursor solution prepared from $Fe(NO_3)_3$, $Sn(OAc)_4$ and Pluronic P123 in *tert*-butanol is spin-coated on different substrates and calcined at 600 °C to produce fully crystalline nanostructured tin-doped hematite films. The films obtained after one coating on a planar substrate are about 60 nm thick, corresponding roughly to a single layer of nanoparticles; the layer thickness can be increased by repeating the coating procedure. Figure 3b shows a SEM cross-section image of a typical Sn:Fe_2O_3 absorber layer obtained by sequential coating of three layers on a planar substrate, reaching a thickness of about 250 nm. The same protocol can be also applied to the impregnation of macroporous scaffolds aimed at the formation of host–guest electrodes, as seen in Figure 3a,c. Simple visual inspection of the images does not suffice to assess the degree of infiltration of tin-doped hematite into the macroporous scaffold. To this end, we have obtained EDX maps acquired in STEM mode on a cross section of the host–guest morphology (Figure 3c). Figure 3d shows a high-resolution TEM image of a few pores. The EDX map shows

DOI: 10.1021/am5078667
ACS Appl. Mater. Interfaces 2015, 7, 4623–4630

excellent agreement between the Sn (turquoise) and Fe (red) rich areas corresponding, respectively, to the scaffold and absorber layer of the underlying TEM image. A large area EDX map across almost the entire thickness of the macroporous film shows successful infiltration of the tin-doped hematite reaching even the bottom pores close to the FTO substrate. We note that some pores, irrespective of their depth within the macroporous film, appear not to be filled, probably because there are inadequate openings to the adjacent pores in the scaffold structure. The hematite particle size in the scaffold is determined to be about 50 nm by TEM, (Figure S 5), which is the same as the particle size of the absorber layer obtained on the flat FTO substrate (Figure 3b), described by us elsewhere.[28]

The absorbance spectra of the three different types of films studied are shown in Figure 4. It can be seen that the scaffold structures have higher absorbance than the "flat" hematite electrode, indicating that the effective optical thickness of the absorber is greater for the same number of coating cycles.

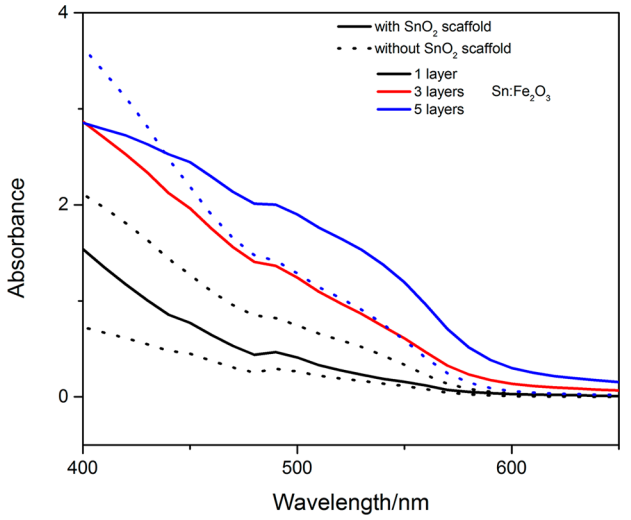

Figure 4. Absorbance spectra of macroporous tin oxide films covered with different numbers of coatings of tin-doped hematite (black: 1 layer; red: 3 layers, blue: 5 layers). Dotted lines: without scaffold; full lines: with scaffold. The absorbance spectra are compared to the ones for the corresponding number of tin-doped hematite coatings on an FTO substrate.

The photocurrent voltage characteristics of tin-doped hematite coatings on the flat substrate (further referred to as a flat absorber layer) as well as the corresponding plots for the tin-doped hematite in the two types of macroporous scaffolds (further referred to as host–guest electrodes) are shown in Figure 5, under AM 1.5 illumination through the substrate or electrolyte (SI or EI, respectively).

SnO_2:Sb host–guest electrodes give the highest dark current, which we attribute to oxygen evolution on the highly conducting scaffold (see Figure S 8). Under SI illumination, the current produced at 1.23 V vs. RHE by the SnO_2:Sb host–guest system is similar to the response of the flat hematite electrode. This indicates that SnO_2:Sb is an appropriate scaffold material for the absorber, but the lack of improvement in the SI photocurrent suggests that electron collection is not limiting the performance of the flat hematite electrode under SI conditions. By contrast, the undoped SnO_2 host–guest electrode produces less current than the flat electrode. This immediately suggests problems with the transfer of electrons from the hematite nanoparticles through the scaffold to the substrate.

Under EI illumination, the situation is quite different, with the SnO_2:Sb host–guest system significantly outperforming the flat electrode. More importantly, the photocurrent density of the host–guest electrode with the SnO_2:Sb scaffold is the same *regardless of the illumination direction*, whereas the photocurrent for the flat electrode is much lower for EI than for SI illumination. We have recently shown[26] that the photocurrent in nanostructured tin-doped hematite is hindered by poor electron collection. The presence of a highly conductive macroporous SnO_2:Sb scaffold evidently lifts this limitation. The Sb doping is clearly the key here, because the SnO_2 host–guest system shows almost no photocurrent for EI illumination, indicating that electron collection is very inefficient.

In order to clarify the role of electronic communication between the absorber layer and the FTO, insulating SiO_2 host–guest structures were prepared with the same macroporous

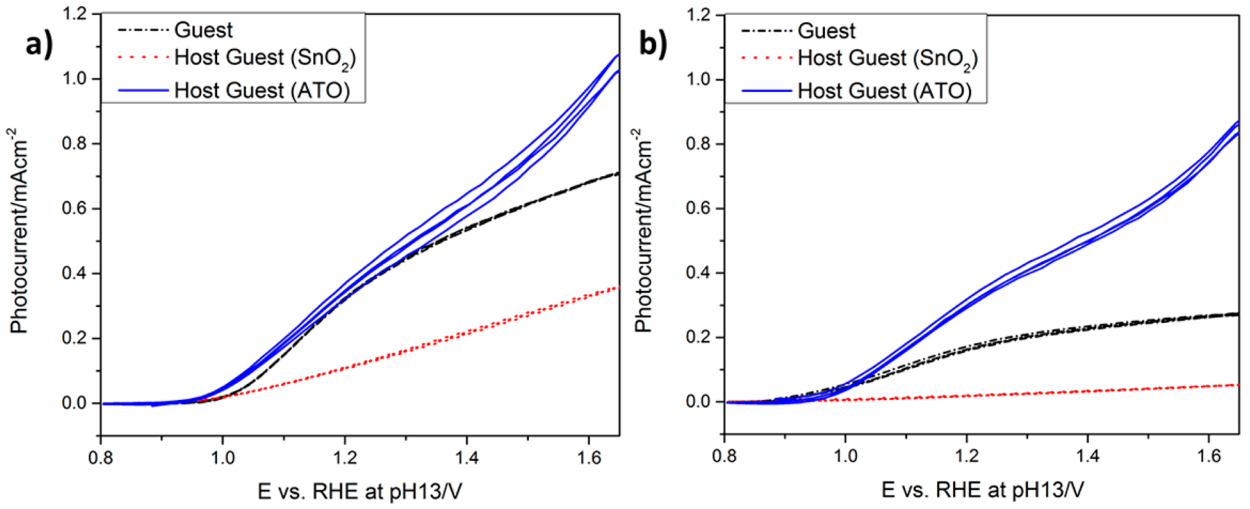

Figure 5. Cyclic voltammetry curves for tin-doped hematite absorber films on flat FTO (dot-dash) or on macroporous SnO_2 (red dots)/SnO_2: Sb (blue line) host–guest scaffolds. In (a) the films were illuminated through the substrate (SI) and in (b) through the electrolyte side (EI) under AM 1.5 conditions. Two repeated scans are shown for each sample.

DOI: 10.1021/am5078667
ACS Appl. Mater. Interfaces 2015, 7, 4623–4630

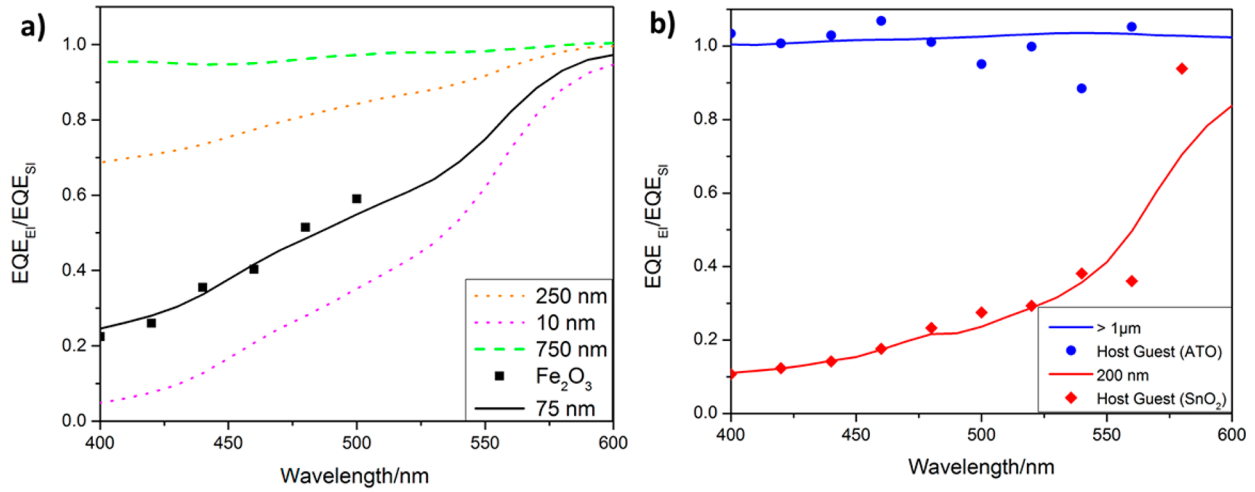

Figure 6. Ratio of EQE measured from the electrolyte and substrate side of (a) flat absorber layer (black squares) and (b) SnO_2 (red diamonds) and SnO_2:Sb (blue points)-based host−guest photoanodes. In (a), theoretical traces of the EQE ratios for different electron diffusion lengths are given, as indicated in the figure. The data points are fitted according to the model of Södergren et al.,[34] suggesting an electron diffusion length of 75 nm for the flat Fe_2O_3 absorber layer, an increased electron diffusion length of 200 nm for the SnO_2 host−guest system, and a diffusion length larger than the film thickness itself for the SnO_2:Sb host−guest system.

morphology. Only a very small photocurrent is detected for these samples, regardless of illumination direction. This indicates that the interconnectivity between the hematite particles in the nanostructure is weak because electron collection involves tortuous pathways where recombination can occur. This contrasts with the situation in the scaffold structures, where the electrons can easily move through the conducting oxide scaffold to the contact.

Light absorption in a nonscattering material can be described in terms of a characteristic penetration depth $1/\alpha(\lambda)$, where $\alpha(\lambda)$ is the wavelength dependent absorption coefficient. The attenuation of the incident illumination as it passes into a semiconductor results in a wavelength dependence of the charge photogeneration profile. For short wavelengths, the majority of the incident radiation is absorbed close to the surface through which light enters. It follows that for EI illumination, the majority of electron−hole pairs are generated far away from the substrate contact. In those cases where the short wavelength EQE is lower for EI than SI illumination, one can conclude that electrons generated on the electrolyte side of the film are lost during transit to the substrate. The problem is simplified if electron transport is by diffusion (i.e., the driving force is primarily due to a concentration gradient rather than an electric field). If under these conditions the loss of electrons can be described by a first order electron lifetime, τ_n, one can use the steady state solutions of the continuity equation given by Södergren et al.[34] The solutions for SI and EI illumination allow for the determination of the electron collection length $L_n = (D_n\tau_n)^{1/2}$ from the ratio of external quantum efficiency spectra recorded for EI and SI illumination. Here D_n is the diffusion coefficient of electrons. This model has been applied to measure the electron diffusion lengths in mesoporous TiO_2[35] and WO_3[36] during light driven water oxidation, although it is not clear what the "recombination" mechanism is nor why the rate should be first order in electron concentration.

The experimental EQE_{EI}/EQE_{SI} data were fitted to the expression derived by Södergren et al.

$$\frac{EQE_{EI}}{EQE_{SI}} = -\frac{(1-R_{EI})[(L\alpha+1)e^{2d/L} - 2L\alpha e^{\alpha d + d/L} + L\alpha - 1]}{(1-R_{SI})[(L\alpha-1)e^{\alpha d+2d/L} + (L\alpha+1)e^{\alpha d} - 2L\alpha e^{d/L}]} \quad (2)$$

Here, R_{EI} and R_{SI} are the reflectances measured through the electrolyte and substrate side, respectively, $\alpha(\lambda)$ is the optical absorption coefficient, d is the film thickness, and L_n is the only fitting parameter. Figure 6a shows the ratio of the EQE measured under illumination through the electrolyte and substrate for a 250 nm thick flat Fe_2O_3 layer on FTO. Also shown are fits to equation 2 for various values of the L_n.

Figure 6b shows the same analysis made on the host−guest films. In the case of the SnO_2 scaffold, the EQE_{EI}/EQE_{SI} ratio can be fitted to an effective electron collection length of 200 nm. Given a film thickness of over a micron, this poor electron collection is consistent with the poor performance of these films, particularly for EI illumination, which is likely to be the most suitable geometry for practical application. SnO_2:Sb-based host−guest films, in contrast, exhibit a EQE_{EI}/EQE_{SI} ratio close to unity over the whole wavelength range, indicating that electron collection is very efficient. This result is consistent with the photocurrent−voltage curves shown in Figure 5a and b, which demonstrate that the photocurrent is independent of the illumination direction for SnO_2:Sb-based host−guest films. We conclude that macroporous SnO_2:Sb makes a very good scaffold for nanostructured tin-doped hematite absorber coatings, particularly for illumination from the electrolyte side. Under SI illumination, in contrast, the SnO_2:Sb host−guest films produce photocurrents very similar to those of flat absorber layer films. Evidently electron collection is not an important limitation when electron hole pairs are generated close to the substrate.

The preceding analysis has been applied elsewhere in the literature[34−36] without a critical examination of why majority carriers (electrons) should be lost in transit to the substrate. In the case of a bulk n-type semiconductor/electrolyte junction, electron hole pairs are separated by the gradient of their respective quasi Fermi levels. Electrons move away from the interface into the bulk region where the electric field is very small (the so-called quasi-neutral region). Here the hole density

DOI: 10.1021/am5078667
ACS Appl. Mater. Interfaces 2015, 7, 4623−4630

is vanishingly small, and there is no route by which electrons can be lost.

This work has shown that deposition of mesoporous hematite layers onto conducting scaffolds to form host–guest architectures significantly improves the electron collection resulting in higher photocurrents compared to planar hematite electrodes. The best results were obtained using antimony-doped SnO_2 as the scaffold. In this case, electron transport is evidently so rapid that electron collection is complete. In a nanostructured electrode, the situation differs from the dense bulk electrode case because the electrolyte permeates into the structure and the semiconductor electrolyte interface extends throughout the layer. This means that electrons in transit to the anode contact have to pass through regions where holes have accumulated at the semiconductor electrolyte interface as a result of the sluggish kinetics for oxygen evolution. In addition to mobile holes, there may be surface bound species such as surface-trapped holes or intermediates in the water oxidation reaction. These act as sinks for the electrons moving toward the contact. The observation that the loss of electrons appears to be adequately characterized by a first order lifetime is surprising. It implies that the concentration of holes (or other species that can capture electrons) is in large excess so that the recombination becomes first order. This is clearly the case in the dye-sensitized solar cell, where the electron acceptor (tri-iodide) is indeed in large excess. The reason for the first order behavior in our case may be that the kinetics governing the consumption of holes in the water splitting reaction are so slow that a large density of holes builds up near the hematite/solution interface. This is consistent with the observation of a persistent photoinduced absorption in hematite that is attributed to holes.[37]

If we follow this line of argument, then we must conclude that electrons escape more easily if the scaffold is highly conducting. The relative widths of the space charge region in the two scaffolds at 1.23 V vs RHE can be estimated from the Mott–Schottky data. In the case of undoped SnO_2, the width of the space charge region is expected to around 30 times thicker than in the case of the antimony-doped scaffold. This means that the quasineutral "core" of the scaffold structure is squeezed into a very small volume, increasing the resistivity of the structure to such an extent that electron transport is slowed down significantly, enhancing the chance of electrons being lost in transit. This interpretation is supported by the almost linear photocurrent voltage plots observed for the undoped scaffold (Figure 3) which suggests a significant *iR* drop. In the antimony-doped SnO_2, on the other hand, the space charge regions will be much thinner, probably only a few nm, leaving a wider highly conducting quasi-neutral core that allows much more rapid transport of electrons to the contact, thus escaping recombination. These are complex systems that are difficult to model, but the qualitative picture described here is a first step toward understanding why highly doped tin oxide frameworks can collect electrons efficiently.

CONCLUSION

The utility of host–guest scaffold photoanodes for water splitting clearly depends on the ability of the scaffold to collect photogenerated electrons. In the case of the highly doped SnO_2, field driven collection of electrons involves rapid movement of electrons in quasi-neutral channels. However, the formation of depletion layers in the undoped SnO_2 scaffold appears to lead to problems under conditions in which the width of the space charge region becomes comparable with the thickness of the scaffold structure. Indeed, under some conditions, penetration of the electric field into the scaffold may no longer occur due to complete depletion of the structure. Electron collection would then involve diffusion, with no contribution from drift. This effect manifests itself most strongly when electron-hole pairs are generated predominantly close to the electrolyte interface, as is the case for illumination from the electrolyte side. The slowing down of electron transport leaves electrons vulnerable to loss by recombination. These problems can be overcome if a highly conducting scaffold is used. In this case electron collection is so rapid that negligible losses occur when electrons move to the substrate contact. Under these conditions, electron collection is efficient even when the electrode is illuminated from the electrolyte side. The highly doped scaffolds used here could therefore find application in devices for light-driven water splitting.

ASSOCIATED CONTENT

Supporting Information

Detailed information regarding XRD, SEM and electrochemical characterization of the host–guest architectures is provided in the Supporting Information. This material is available free of charge via the Internet at http://pubs.acs.org.

AUTHOR INFORMATION

Corresponding Author

*E-mail: bein@lmu.de.

Author Contributions

⊥I.K. and H.K.D. contributed equally

Notes

The authors declare no competing financial interest.

ACKNOWLEDGMENTS

The work was supported by the German Research Foundation, DFG (SPP 1613), the Nanosystems Initiative Munich (NIM) and LMUexcellent funded by the DFG, the Bavarian research network "Solar Technologies Go Hybrid", and the Center for Nanoscience (CeNS). We thank the students Bernhard Böller and Jonathan Kampmann who participated in the research.

REFERENCES

(1) Sivula, K.; Le Formal, F.; Grätzel, M. Solar Water Splitting: Progress Using Hematite (α-Fe_2O_3) Photoelectrodes. *ChemSusChem* **2011**, *4*, 432–449.

(2) Grätzel, M. Photoelectrochemical Cells. *Nature* **2001**, *414*, 338–344.

(3) Hara, M.; Kondo, T.; Komoda, M.; Ikeda, S.; N. Kondo, J.; Domen, K.; Hara, M.; Shinohara, K.; Tanaka, A. Cu_2O as a Photocatalyst for Overall Water Splitting Under Visible Light Irradiation. *Chem. Commun.* **1998**, *3*, 357–358.

(4) Sivula, K.; Zboril, R.; Le Formal, F.; Robert, R.; Weidenkaff, A.; Tucek, J.; Frydrych, J.; Grätzel, M. Photoelectrochemical Water Splitting with Mesoporous Hematite Prepared by a Solution-Based Colloidal Approach. *J. Am. Chem. Soc.* **2010**, *132*, 7436–7444.

(5) Bolton, J. R.; Strickler, S. J.; Connolly, J. S. Limiting and Realizable Efficiencies of Solar Photolysis of Water. *Nature* **1985**, *316*, 495–500.

(6) Dare-Edwards, M. P.; Goodnough, J. P.; Hamnett, A.; Trevellick, P. R. Electrochemistry and Photoelectrochemistry of Iron(III) Oxide. *J. Chem. Soc., Faraday Trans.* **1983**, *79*, 2027–2041.

(7) Kennedy, J. H.; Frese, K. W. Photooxidation of Water at α-Fe_2O_3 Electrodes. *J. Electrochem. Soc.* **1978**, *125*, 709–714.

DOI: 10.1021/am5078667
ACS Appl. Mater. Interfaces 2015, 7, 4623–4630

(8) Fu, Y.; Chen, J.; Zhang, H. Synthesis of Fe_2O_3 Nanowires by Oxidation of Iron. *Chem. Phys. Lett.* **2001**, *350*, 491−494.
(9) Mushove, T.; Blodgett, S.; Thompson, L. T. Design, Design, Synthesis, and Characterization of Hematite Nanotubes for Photoelectrochemical Water Splitting. *Meeting Abstracts* **2013**, *MA2013−02*, 2541.
(10) Tilley, S. D.; Cornuz, M.; Sivula, K.; Grätzel, M. Light-Induced Water Splitting with Hematite: Improved Nanostructure and Iridium Oxide Catalysis. *Angew. Chem., Int. Ed.* **2010**, *49*, 6405−6408.
(11) Fu, Y.; Chen, J.; Zhang, H. Synthesis of Fe_2O_3 Nanowires by Oxidation of Iron. *Chem. Phys. Lett.* **2001**, *350*, 491−494.
(12) Yuan, L.; Wang, Y.; Cai, R.; Jiang, Q.; Wang, J.; Li, B.; Sharma, A.; Zhou, G. The Origin of Hematite Nanowire Growth During the Thermal Oxidation of Iron. *Mater. Sci. Eng., B* **2012**, *177*, 327−336.
(13) LaTempa, T. J.; F, X.; Paulose, M.; Grimes, C. A. Temperature-Dependent Growth of Self-Assembled Hematite (α-Fe_2O_3) Nanotube Arrays: Rapid Electrochemical Synthesis and Photoelectrochemical Properties. *J. Phys. Chem. C* **2009**, *113*, 16293−16298.
(14) Cesar, I.; Sivula, K.; Kay, A.; Zboril, R.; Graetzel, M. Influence of Feature Size, Film Thickness, and Silicon Doping on the Performance of Nanostructured Hematite Photoanodes for Solar Water Splitting. *J. Phys. Chem. C* **2009**, *113*, 772−782.
(15) Itoh, K. B.; J.O'M. Thin Film Photoelectrochemistry: Iron Oxide. *J. Electrochem. Soc.* **1984**, *131*, 1266−1271.
(16) Sivula, K.; Formal, F. L.; Grätzel, M. WO_3−Fe_2O_3 Photoanodes for Water Splitting: A Host Scaffold, Guest Absorber Approach. *Chem. Mater.* **2009**, *21*, 2862−2867.
(17) Wang, L.; Palacios-Padrós, A.; Kirchgeorg, R.; Tighineanu, A.; Schmuki, P. Enhanced Photoelectrochemical Water Splitting Efficiency of a Hematite−Ordered Sb:SnO_2 Host−Guest System. *ChemSusChem* **2014**, *7*, 421−424.
(18) Sun, Y.; Chemelewski, W. D.; Berglund, S. P.; Li, C.; He, H.; Shi, G.; Mullins, C. B. Antimony-Doped Tin Oxide Nanorods as a Transparent Conducting Electrode for Enhancing Photoelectrochemical Oxidation of Water by Hematite. *ACS Appl. Mater. Interfaces* **2014**, *6*, 5494−5499.
(19) Qiu, Y.; Leung, S.-F.; Zhang, Q.; Hua, B.; Lin, Q.; Wei, Z.; Tsui, K.-H.; Zhang, Y.; Yang, S.; Fan, Z. Efficient Photoelectrochemical Water Splitting with Ultrathin films of Hematite on Three-Dimensional Nanophotonic Structures. *Nano Lett.* **2014**, *14*, 2123−2129.
(20) Riha, S. C.; DeVries Vermeer, M. J.; Pellin, M. J.; Hupp, J. T.; Martinson, A. B. F. Hematite-based Photo-oxidation of Water Using Transparent Distributed Current Collectors. *ACS Appl. Mater. Interfaces* **2013**, *5*, 360−367.
(21) Stefik, M.; Cornuz, M.; Mathews, N.; Hisatomi, T.; Mhaisalkar, S.; Grätzel, M. Transparent, Conducting Nb:SnO_2 for Host−Guest Photoelectrochemistry. *Nano Lett.* **2012**, *12*, 5431−5435.
(22) Young Kim, J.; Jang, J.-W.; Hyun Youn, D.; Yul Kim, J.; Sun Kim, E.; Sung Lee, J. Graphene-Carbon Nanotube Composite as an Effective Conducting Scaffold to Enhance the Photoelectrochemical Water Oxidation Activity of a Hematite Film. *RSC Adv.* **2012**, *2*, 9415−9422.
(23) Le Formal, F.; Grätzel, M.; Sivula, K. Controlling Photoactivity in Ultrathin Hematite Films for Solar Water-Splitting. *Adv. Funct. Mater.* **2010**, *20*, 1099−1107.
(24) Hisatomi, T.; Dotan, H.; Stefik, M.; Sivula, K.; Rothschild, A.; Grätzel, M.; Mathews, N. Enhancement in the Performance of Ultrathin Hematite Photoanode for Water Splitting by an Oxide Underlayer. *Adv. Mater.* **2012**, *24*, 2699−2702.
(25) Wang, D.; Zhang, Y.; Wang, J.; Peng, C.; Huang, Q.; Su, S.; Wang, L.; Huang, W.; Fan, C. Template-Free Synthesis of Hematite Photoanodes with Nanostructured ATO Conductive Underlayer for PEC Water Splitting. *ACS Appl. Mater. Interfaces* **2013**, *6*, 36−40.
(26) Mandlmeier, B.; Minar, N. K.; Feckl, J. M.; Fattakhova-Rohlfing, D.; Bein, T. Tuning the Crystallinity Parameters in Macroporous Titania Films. *J. Mater. Chem. A* **2014**, *2*, 6504−6511.
(27) Fried, D. I.; Ivanova, A.; Muller, V.; Rathousky, J.; Smarsly, B. M.; Fattakhova-Rohlfing, D. A Facile Synthesis of Mesoporous Crystalline Tin Oxide Films Involving a Base-Triggered Formation of Sol-Gel Building Blocks. *Nanoscale* **2011**, *3*, 1234−1239.
(28) Dunn, H. K.; Feckl, J. M.; Müller, A.; Fattakhova-Rohlfing, D.; Peter, L. M.; Scheu, C.; Bein, T. Tin Doping Speeds Up Hole Transfer During Light-Driven Water Oxidation at Hematite Photoanodes. *Phys. Chem. Chem. Phys.* **2014**, *16*, 24610−24620.
(29) Schuster, J.; He, G.; Mandlmeier, B.; Yim, T.; Lee, K. T.; Bein, T.; Nazar, L. F. Spherical Ordered Mesoporous Carbon Nanoparticles with High Porosity for Lithium−Sulfur Batteries. *Angew. Chem., Int. Ed.* **2012**, *51*, 3591−3595.
(30) Strecker, A.; Salzberger, U.; Mayer, J. Specimen Preparation for Transmission Electron Microscopy: Reliable Methods for Cross-Sections and Brittle Materials. *Prakt. Metallogr.* **1993**, *30*, 482−495.
(31) Klahr, B. M.; Martinson, A. B. F.; Hamann, T. W. Photoelectrochemical Investigation of Ultrathin Film Iron Oxide Solar Cells Prepared by Atomic Layer Deposition. *Langmuir* **2011**, *27*, 461−468.
(32) Li, F.; Josephson, D. P.; Stein, A. The Road from Particles to Colloidal Molecules and Crystals. *Angew. Chem., Int. Ed.* **2010**, *50*, 360−388.
(33) Frydrych, J.; Machala, L.; Tucek, J.; Siskova, K.; Filip, J.; Pechousek, J.; Safarova, K.; Vondracek, M.; Seo, J. H.; Schneeweiss, O.; Gratzel, M.; Sivula, K.; Zboril, R. Facile Fabrication of Tin-Doped Hematite Photoelectrodes - Effect of Doping on Magnetic Properties and Performance for Light-Induced Water Splitting. *J. Mater. Chem.* **2012**, *22*, 23232−23239.
(34) Södergren, S.; Hagfeldt, A.; Olsson, J.; Lindquist, S. E. Theoretical Models for the Action Spectrum and the Current-Voltage Characteristics of Microporous Semiconductor Films in Photoelectrochemical Cells. *J. Phys. Chem.* **1994**, *98*, 5552−5555.
(35) Leng, W. H.; Barnes, P. R. F.; Juozapavicius, M.; O'Regan, B. C.; Durrant, J. R. Electron Diffusion Length in Mesoporous Nanocrystalline TiO_2 Photoelectrodes During Water Oxidation. *J. Phys. Chem. Lett.* **2010**, *1*, 967−972.
(36) Wang, H.; Lindgren, T.; He, J.; Hagfeldt, A.; Lindquist, S.-E. Photoelectrochemistry of Nanostructured WO_3 Thin Film Electrodes for Water Oxidation: Mechanism of Electron transport. *J. Phys. Chem. B* **2000**, *104*, 5686−5696.
(37) Le Formal, F.; Pendlebury, S. R.; Cornuz, M.; Tilley, S. D.; Grätzel, M.; Durrant, J. R. Back Electron-Hole Recombination in Hematite Photoanodes for Water Splitting. *J. Am. Chem. Soc.* **2014**, *136*, 2564−2574.

DOI: 10.1021/am5078667
ACS Appl. Mater. Interfaces 2015, 7, 4623−4630